

# A Porphyrin-Based Molecular Cage Guided by Designed Local-Electric Field Is Highly Selective and Efficient

Shakir Ali Siddiqui<sup>1</sup>, Sason Shaik<sup>2\*</sup>, Surajit Kalita<sup>1</sup> and Kshatresh Dutta Dubey<sup>1\*</sup>

1. Department of Chemistry, School of Natural Sciences, Shiv Nadar Institution of Eminence Delhi-NCR.
2. Institute of Chemistry, The Hebrew University of Jerusalem Israel, Jerusalem, Israel.

\* [sason@yfaat.ch.huji.ac.il](mailto:sason@yfaat.ch.huji.ac.il), [kshatresh.dubey@snu.edu.in](mailto:kshatresh.dubey@snu.edu.in),

## Abstract:

The present work outlines a general methodology for designing efficient catalytic machineries that can easily be tweaked to meet the demands of the target reactions. This work utilizes a principle of the designed local electric field (LEF) as the driver for an efficient catalyst. It is demonstrated that by tweaking the LEF, we can catalyze the desired hydroxylation products with enantioselectivity that can be changed at will. Using computation tools, we caged a synthetic analog of heme porphyrin (HM1) and investigated the pharmaceutically relevant conversion of Tetralin to Tetralol, inside the modified supramolecular cage. The QM/MM calculations demonstrate a resulting catalytic efficiency with virtually absolute *Pro-R* selectivity for the tetralin hydroxylation. Our calculations show that the LEF of the supramolecular cage and *HM1* exerts a strong electric field along the *Fe—O* reaction axis, which is the main driving force for enhanced reactivity. At the same time, the supramolecular cage applies a lateral LEF that regulates the enantioselectivity. We further demonstrate that swapping the charged/polar substitution in the supramolecular cage switches the lateral LEF which changes the enantioselectivity of hydroxylation from *R* to *S*.

## 1. Introduction

We outline here a general methodology for designing efficient catalysts that can easily be tweaked to meet the demands of the target reactions. The work utilizes computational design principles<sup>1-5</sup> towards this goal. The principles are then applied to design a supramolecular cage that possesses an efficient scaffold, which can be easily modified to catalyze the formation of desired hydroxylation products with enantioselectivity at will.

There exist two major requirements in such catalyst design; (a) establishing a methodology for tailoring the requisite scaffold, and (b) codifying the essential descriptor that effects the requisite catalysis<sup>6-8</sup>. While enzymes could serve as initial scaffolds, their low thermal stabilities<sup>9,10</sup> and tolerance towards the organic solvents<sup>11,12</sup> make them inapt and requires an extensive random mutation in the protein matrix<sup>13-15</sup>. Viable alternatives are supramolecular complexes, such as organic cages, which are smaller than enzymes, while possessing active-site architectures akin to enzymes<sup>16-19</sup>. Herein, we describe such a supramolecular cage.

The electrostatic field of the supramolecular cage is an ideal choice of a catalytic effector<sup>20</sup>. Thus, it is well established that the preorganization of the charged functional group in the enzymatic system is responsible for enzyme catalysis<sup>21</sup>. Indeed, recent studies by several groups have shown that the local electric fields (LEFs) of enzymes and/or solvents constitute the main catalytic elements for several reactions<sup>22-28</sup>. This fact is supported by several recent studies where the application of oriented external electric field (OEEF)<sup>29-31</sup> along the “reaction axis” significantly enhances the rate of reactions and controls their product selectivity<sup>32-39</sup>. As such, the LEF along the reaction axis can be used as an effector of the catalytic activity<sup>27</sup> in our target cages. Herein we demonstrate that a methodological design of LEF in a supramolecular cage brings about the desired reactivity and selectivity of C-H hydroxylation reactions.

**The Model System:** Our choice of initial catalyst is a synthetic porphyrin derivative, **HM1** in Figure 1A, which was developed by Groves et al.<sup>40</sup> and demonstrated to enhance hydrogen abstraction reactions in aqueous solutions. The rate-enhancement capability of **HM1** was later shown to originate in the LEF of the charged peripheral substituents.<sup>22</sup>

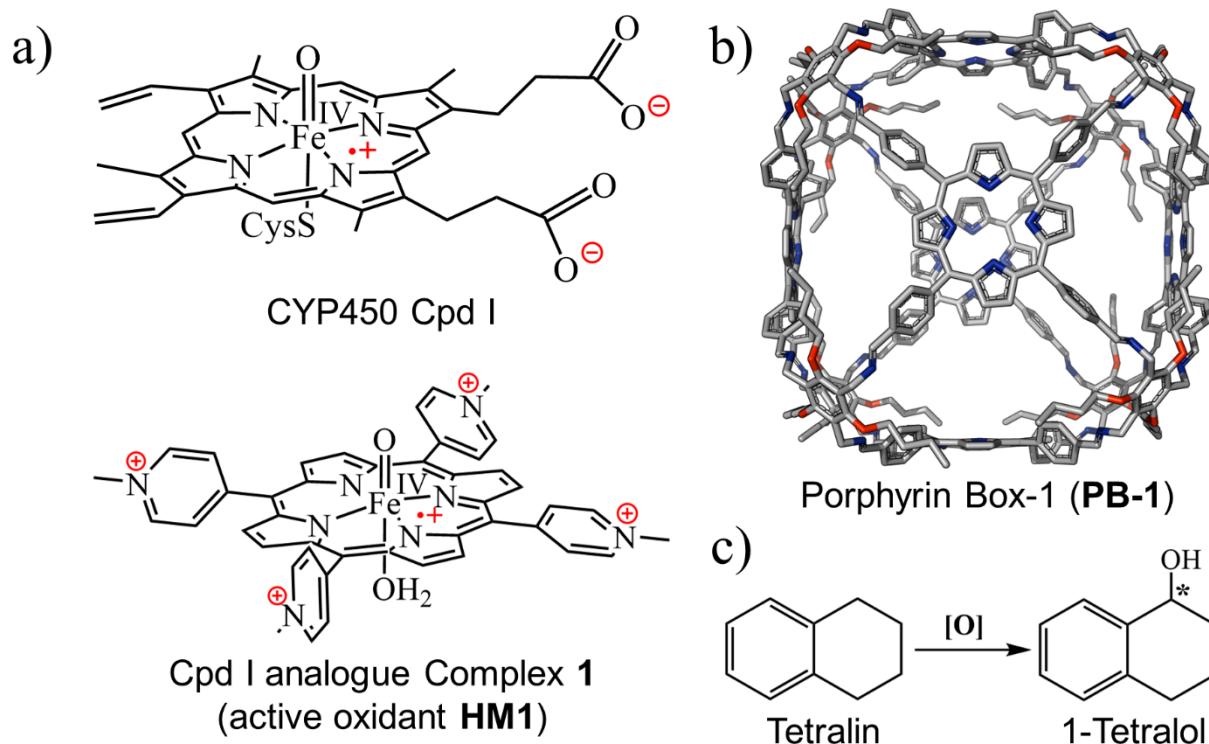


**Figure 1.** (a) The active oxidant Cpd I in the catalytic cycle of P450s and its analogue Complex 1, here referred as **HM1**. (b) Porphyrin box-1 (**PB-1**), initial skeleton used in the study. Hydrogens are omitted for clarity. (c) Chemical structure of tetralin and Tetralol.

For the supramolecular scaffold, we selected the porous organic cage (Figure 1b), which was synthesized by Kim et al, and named porphyrin box, **PB-1**<sup>17</sup>. As was shown by Kim et al, **PB-1** possesses exceptional chemical stability and applicability; including selective gas sorption, encapsulation of guest molecules, etc. Importantly, such porous organic cages were reported to preserve their stability even after post-synthetic modification<sup>41–43</sup> of some functional groups of such cages. Therefore, we deem this supramolecular scaffold to be an ideal starting platform that can be selectively modified (see SI, Figure S1, S2) for tailoring the LEF along the reaction axis of **HM1**, as well as for encapsulating target substrates for oxidation.

As a substrate that can be used to explore reactivity and selectivity, we chose the conversion of Tetralin to Tetralol (Figure 1c), which involves both C-H hydroxylation and enantio-selectivity of the product. Thus, (*R*)-1-Tetralol is extensively used to treat several disorders such as obsessive-compulsive disorder, post-traumatic stress, premenstrual dysphoric disorder, and social anxiety<sup>44-46</sup>. Can the chosen cage produce (*R*)-1-Tetralol? Can it produce, on demands, also (*S*)-1-Tetralol?

As shown in the foregoing sections, we can tailor the magnitude of the LEF as well as its specific orientation and produce a supramolecular cage that enhances reactivity and enantioselectivity.

## 2. Computational Details:

In the present study, we used MD simulations for the entrapment, conformational and binding stabilities of TLN & HM1 inside the cage, QM/ MM calculations for the mechanism and electronic structure investigations, quantification of the local electric field and QM-only DFT calculations to study the effect of the oriented external electric field (OEEF) onto the reaction axis. The details of each method are described below:

### 2.1. System Preparation:

We chose the porous organic cage, created by Kim et al.<sup>17</sup> and known as porphyrin box PB-1, for the initial supramolecular scaffold, and modelled it for entrapment of substrate and stability of HM1 using the flowchart in Figure 2. The detailed description of the modelling procedure is discussed in Text S1 of the supplementary material. Interestingly, such post synthetic substitutions and insertion of the covalent groups in the cage has been validated in experiments by Yusran et al.<sup>42</sup> The PB-1 was optimized with AM1 semi-empirical theory<sup>47</sup>. The parameters for PB-1 cage were generated using the antechamber module of Amber20 for GAFF2

parameters<sup>48</sup> for a QM-optimized geometry at the AM1 level of theory. The parameters for oxidant HM1 were prepared by the MCPB.py program, a python-based metal parameter builder used to generate a forcefield for the metal center of the protein, employing the bonded model approach<sup>49</sup>. Again, the partial atomic charges and missing parameters for tetralin (TLN) substrate were obtained from the RESP charge fitting method for the QM-optimized geometry at the HF/6-31G\* level of theory<sup>50,51</sup>. After docking the HM1 & TLN inside the so-created cages, all the complexes were solvated in a rectangular box of CHCl<sub>3</sub> solvent molecules with a 10 Å cutoff from the supramolecular cage boundary using the CHCl<sub>3</sub>BOX using leap module. A suitable quantity of Cl<sup>-</sup> ions were supplied to balance out the system's overall charge in each case.

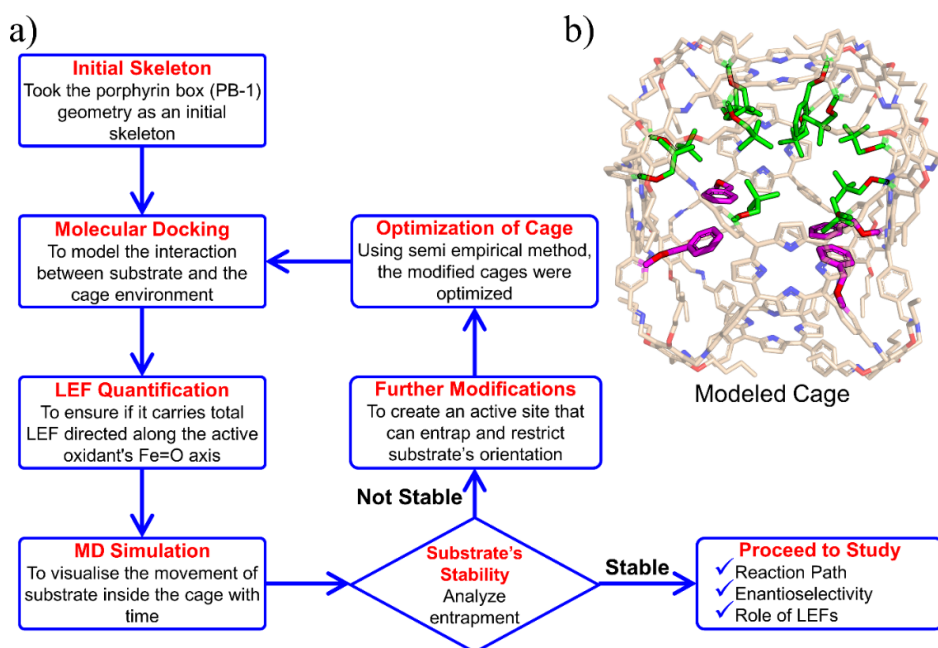


**Figure 2.** (a) A flowchart of the protocol to engineer the porphyrin box for the substrate and active oxidant HM1. (b) Modeled Cage, here modifications are highlighted in green.

## 2.2. MD Simulations:

The various systems were minimized in two phases after the complexes were initially built up to get rid of the poor connections. In step 1, only solvent molecules were minimized using the

conjugate gradient minimizer after 5000 steps of the steepest descent. Using the same minimizer, as in step 1, all of the complexes were minimized in step 2 without any constraints.

All the systems were then gently equilibrated from 10 to 300 K under the NVT ensemble for 50 ps with a weak restraint of 5 kcal mol<sup>-1</sup>Å<sup>-2</sup>. Subsequently, a density equilibrium was performed using the NPT ensemble at a targeted temperature of 300 K and pressure of 1 atm for 1 ns using the Langevin thermostat<sup>52</sup> and the Berendsen barostat,<sup>53</sup> with a weak restraint of 1 kcal mol<sup>-1</sup>Å<sup>-2</sup>. Following the removal of all restraints, the systems were further equilibrated for 3 ns, and then 100 ns of production simulations for each system were run and the convergence of the simulation is checked. Furthermore, these procedures were replicated three more times. The covalent bonds that contain hydrogens were constrained using the SHAKE algorithm<sup>52</sup>, and a particle mesh Ewald (PME) method<sup>53</sup> was utilized to treat long-range electrostatic interactions during all the MD simulations. The entire simulation was run with an integration step of 2 fs. The Amber20 package's GPU version was used to run all of the MD simulations.<sup>54</sup>

### 2.3. QM/MM Calculations:

The reaction mechanism and the electronic structure were investigated using QM/MM calculations for the snapshot from the MD trajectory. The QM regions included the oxidant **HM1** and the substrate tetralin (TLN), for which the coordinates for the QM region for QM/MM optimized geometry can be found in this SI. The entire supramolecular modeled cage and solvent molecules within 8 Å of HM1 were included in the ‘active region’ of the QM/MM calculations. The atoms in the ‘active region’ interact with the QM atoms through electrostatic and van der Waals interactions and the corresponding polarization effects were considered in the subsequent QM/MM calculations. All the QM/MM calculations were performed using ChemShell<sup>55,56</sup>, by combining Turbomole<sup>57,58</sup> for the QM part and DL\_POLY<sup>59</sup> for the MM part. The MM region was described using the Amber force field generated for cage, and the

electronic embedding scheme was used to account for the polarizing effect of the enzyme environment on the QM region.

During QM/MM geometry optimizations, the QM region was computed using the hybrid UB3LYP functional<sup>60</sup> with the def2-SVP basis set. All of the QM/MM transition states (TSs) were located by relaxed potential energy surface (PES) scans followed by full TS optimizations using the P-RFO optimizer<sup>61</sup> implemented in the HDLC code. The results were further validated with single-point calculations at a higher basis set, def2-TZVP. All calculations were performed for the doublet and sextet states since recent studies showed that the pristine oxidant **HM1** displays two-state reactivity (doublet and sextet spins) in gas phase<sup>62,22</sup>.

#### **2.4. Quantification of the Local Electric Fields (LEFs) and Electrostatic Stabilization Energy:**

The TITAN and TUPÅ codes were used to quantify the local electric fields (LEFs) present in the systems.<sup>23,63,64</sup> Using the TUPÅ code, we quantified the evolution of LEFs for solvated cage, oxidant **HM1** & entire system from whole MD simulation trajectory at 10 ps time intervals, along the reaction axis, (z-axis, Fe=O) as well as the selectivity axis (y-axis). The solvent molecules present in the 3Å vicinity of **HM1** were included. The electric fields along the MD trajectory were measured using the point charge distribution included in the parameter topology file.

For the QM/MM optimized RC and TS geometries, the LEF along both the axes were quantified using in-house TITAN code. The quantification included the charges of methyl pyridinium cationic periphery of **HM1**, entire cage and the solvent molecule near 3Å of **HM1**. Dipole moments were calculated for H<sub>2</sub>O-Fe=O, porphyrin and TLN substrate. Then interaction/stabilization energy were calculated using the following relationship:<sup>31</sup>

$$\Delta E = 4.8|\vec{F}| \cdot |\vec{\mu}| \cdot \cos\theta$$

Here,  $\Delta E$  is stabilization energy in kcal/mol,  $|\vec{F}|$  is the LEF intensity in V/Å, the  $|\vec{\mu}|$  is the magnitude of dipole moment in Debye and  $\theta$  is the angle between LEF and dipole moment vectors. For electric field and dipole moments, GAUSSIAN convention is used.<sup>31,65</sup>

Furthermore, QM-only single point calculations were performed with and without oriented external electric fields (OEEFs) for the stripped RC and TS geometries. For frequency calculations, we used the hybrid UB3LYP/def2-SVP level of theory<sup>60</sup> and single-point calculations at a higher basis set, def2-TZVP. These effects were studied using Gaussian09 program.<sup>66</sup>

## 2.5. Adaptive Steered Molecular Dynamics (ASMD) Simulations:

For efficient catalysis the entry and exit of the substrate/product is crucial, and therefore, we determined the route and feasibility of substrate entry and product escape in the designed cage, using adaptive steered molecular dynamics (ASMD) simulations<sup>54</sup>. In so doing, we applied an external force in a predetermined direction and performed 20 iterative simulations of ASMD by using the end-to-end distance between the iron center of Fe=O and the 'C' of the substrate/product as our reaction coordinate. The adaptive steering was continued along the reaction coordinate from 3 to 23 Å in 10 stages until the substrate/product was entirely outside of the cage. We assigned a spring constant of 10 kcal/mol•Å<sup>2</sup>, and used a velocity of 0.5 Å/ns for simulations of a total duration of 800 ns. Finally, we calculated the potential of mean force (PMF), from entire 800ns of simulation which characterizes the free energy change along a reaction coordinate during different intermediate stages of a product exit using the Jarzynski's equality<sup>67</sup> -

$$\langle \exp(-\beta W) \rangle = \exp(-\beta \Delta G) \quad \dots\dots\dots(1)$$

In equation 1,  $\langle \rangle$  denotes the ensemble average,  $\beta=(k_B T)^{-1}$  ( $k_B$  is Boltzmann constant and  $T$  is temperature),  $W$  is the work done on the system during a non-equilibrium process, and  $\Delta G$  is the difference in free energy between two equilibrium states of the system.

### 3. Results & Discussion:

#### 3.1 Encapsulation of the active oxidant and the substrate inside the modeled cage

Initially we tailored **PB-1** to better fit **HM1** using a protocol shown in Figure 2a. Since the active oxidant **HM1** contains four peripheral pyridinium groups, we anticipated that it could be stabilized in the cage with the aid of  $\pi$ - $\pi$  stacking interactions, and therefore, we introduced phenyl rings inside the walls of **PB-1**. The initial substitution for entrapment of only **HM1** can be found in the SI (figure S1). The simulation of the modified cage and its resident **HM1** substantiates our reasoning that the stability of the complex was mainly driven by  $\pi$ - $\pi$  stacking interactions. Subsequently, we docked the Tetralin substrate in the so modified cage. After a few rounds of subsequent modifications that preserve the stability of **HM1** and the binding of the substrate during simulations (see SI, Figure S2, S3, S4 & S5), we eventually achieved our final ‘modeled cage’ is shown in Figure 2b. Here violet color shows modifications to stabilize **HM1**, while green represents the requisite modifications that stabilize the substrate binding.

***The stability of the substrate and oxidant inside the cage:*** The MD simulations of the substrate and the oxidant in the solvated cage show that three phenyl rings of the cage strongly interact with the three peripheral pyridinium substituents of the porphyrin **HM1** and stabilize it (see Figures 3a). The contact density (Figure 3b) further validates the strong  $\pi$ - $\pi$  stacking interactions with the modified cage and **HM1**. Note that three interactions out of four are occupied for more than 88% of the time below 5Å distance during the simulation, which shows strong  $\pi$ - $\pi$  interactions. Additionally, the root mean square deviation (RMSD) of the modified

cage in the presence of **HM1** and the substrate during the molecular dynamics (MD) simulations is just  $\sim 1\text{\AA}$ , which strongly validates the stability of the host-guest model (see RMSD in figure S4).

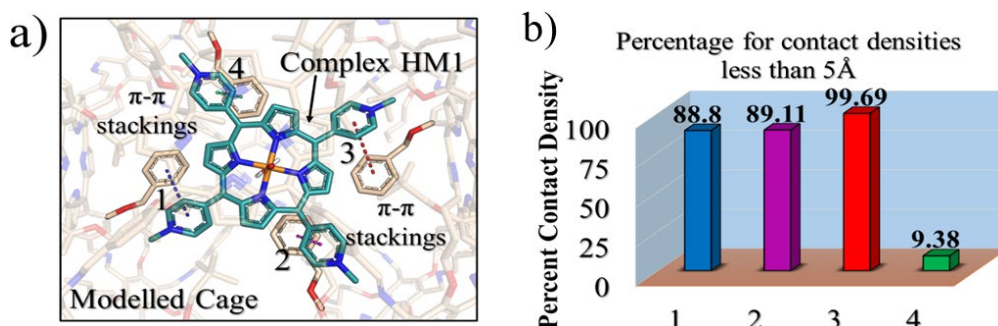


**Figure 3.** (a) A representative MD snapshot illustrating the  $\pi$ - $\pi$  stacking interactions between the inserted **HM1** and the introduced phenyl rings in interior walls of the modeled cage. 1, 2, 3 and 4 represent the four different  $\pi$ - $\pi$  stacking interactions, shown in blue, magenta, red and green, respectively. (b) The percentage for contact densities between **HM1** and four phenyl substitutions.

### 3.2. Testing the Role of the LEF on Reactivity and Selectivity

This section demonstrates that the unusual impact of the cage on reactivity and enantioselectivity originates in the combined LEF of **HM1** and the container **PB1**. This is done by initially evaluating the combined LEF effects on the RC and TS species along the reaction coordinate. Subsequently, we investigate the role of the LEF in determining the special electronic structures of these species. This was complemented by determining the LEF role on the enantioselectivity of the reaction. And finally, by showing that we can get enantioselectivity at will, by simply flipping the direction of the lateral LEF.

**The LEF of the Complex:** Let us quantify the LEF of the complex (solvated **PB1**+**HM1**) along the reaction axis ( $Z$  - direction) and the lateral direction ( $Y$ -axis). Such a 2-dimensional (2D) electric field was demonstrated in the past to bring about reactivity enhancement as well as enantioselectivity.<sup>34</sup> Thus, we expect that the LEF along the  $Z$ -axis affects reactivity while along the  $Y$ -axis, it affects the enantioselectivity. Our analysis in Figure 4 shows the existence of a significant LEF along the Fe-O, i.e.,  $Z$ -axis. This LEF( $Z$ ) is a

combination of the LEFs of the solvated cage and the **HM1**, where the solvated cage contributes  $\sim 0.07$  V/Å and HM1 contributes  $\sim 0.23$  V/Å to the total LEF of  $\sim 0.30$  V/Å. Furthermore, the cage contributes also a significant LEF(Y) in the Y-direction of  $-0.10$  V/Å. As such, the LEF of the cage and HM1 are expected to play a significant role in the reactivity and enantioselectivity of the oxidation reaction.

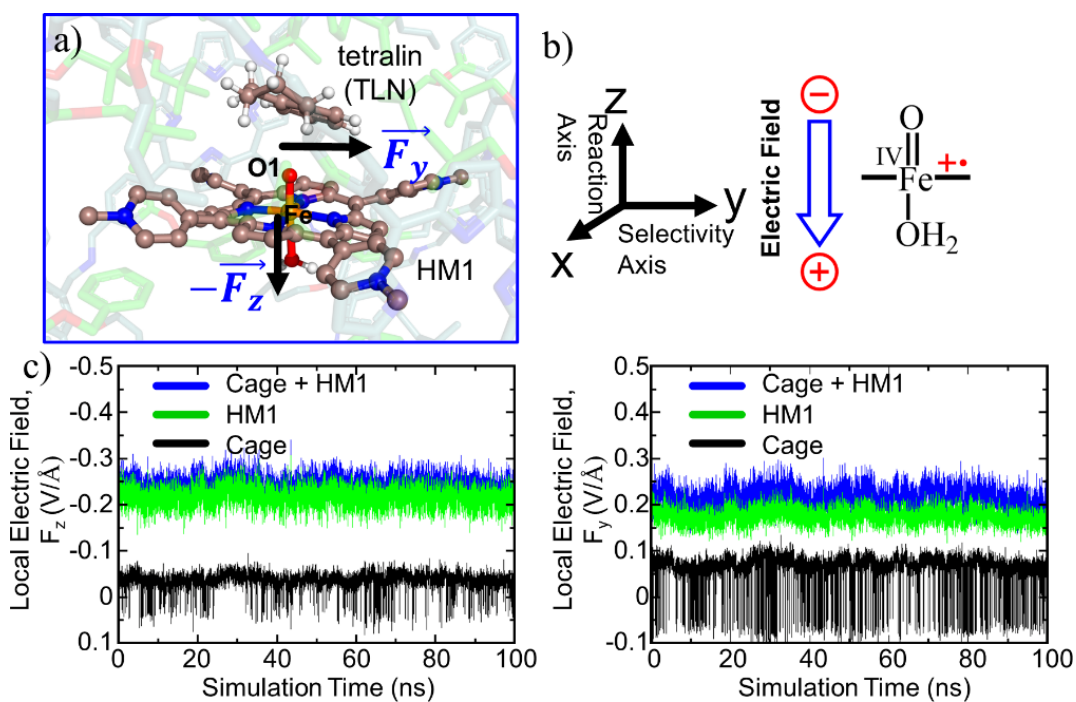


**Figure 4.** (a) A representative MD snapshot highlighting the reactive complex inside the cage. (b) Reaction axis & electric field direction, GAUSSIAN convention is used. (c) The Local Electric Field (LEF) along y- and z- axis with evolution of time.

While oxidant **HM1** is known to be intrinsically reactive in H-atom-transfer (HAT) reactions<sup>22,40,62</sup>, the enantioselectivity has not been explored. As can be seen from Figure 5a which represents a snapshot from 100 ns MD simulation, the substrate occupies a very a close position to the oxidant, and both pro-*R* and pro-*S* hydrogen atoms are also in the proximity of the oxo-iron moiety of **HM1**. The proximities of these hydrogen atoms are also persistent throughout the simulations which can be verified by the distance vs. time plot (Figure 5b) and the plot of distance vs population (Figure 5c). At the same time, it is apparent that the pro-*R* hydrogen is closer than the pro-*S* one. As mentioned earlier, hydroxylation of tetralin at pro-*R*

position has medicinal importance<sup>44</sup>. It is noteworthy that our modeled system gives a clear preference for *pro-R* selectivity, and is thus of industrial relevance.

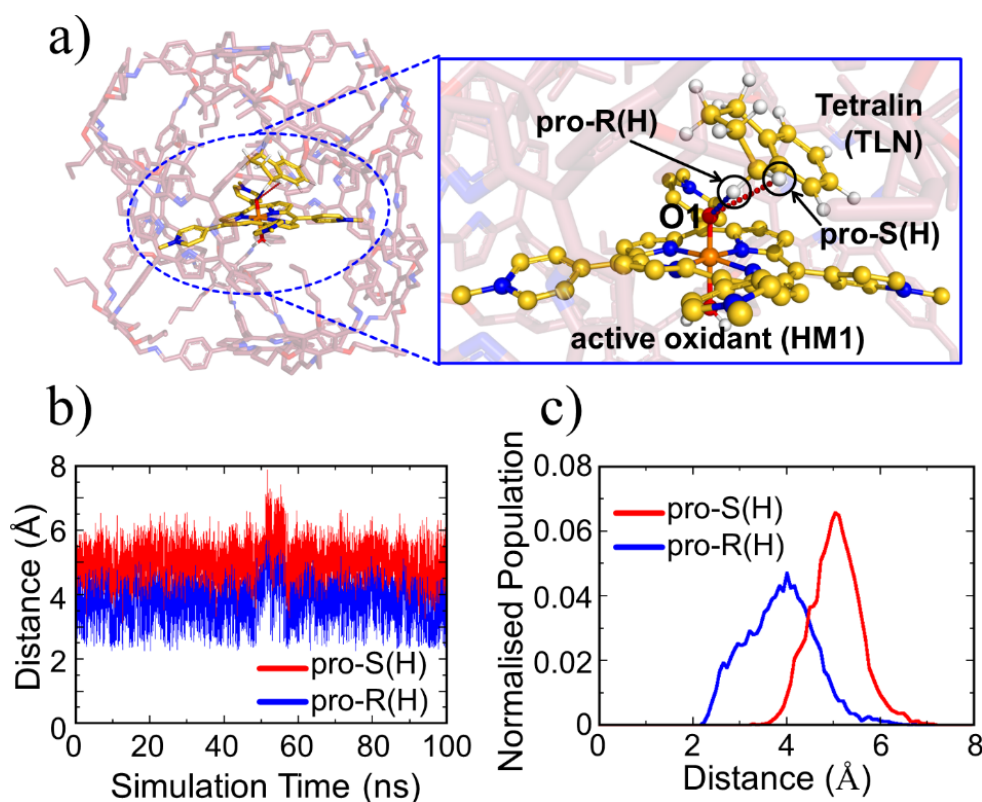


**Figure 5.** (a) A representative MD snapshot unveiling the *pro-R* and *pro-S* hydrogens of the substrate tetralin (TLN). (b) Distance plots between these hydrogens and O1 atom of the oxidant (HM1). (c) The Boltzmann population of the *pro-R* and *pro-S* hydrogens distances (from the oxo atom of Fe=O) over the entire 100 ns MD simulation.

**QM/MM Calculations during the Reaction Course:** To validate the kinetic feasibility of the *R*-enantioselective reaction, we performed QM/MM calculations, using the most populated snapshot based on Boltzmann population distribution<sup>\*</sup>, followed by potential energy scan along the H-abstraction pathway. Furthermore, since recent investigations<sup>22</sup> revealed that the pristine oxidant HM1 exhibits two-state reactivity (doublet and sextet spins) in its gas phase reaction with methane, we investigate the reactivity of the two spin states. Our

<sup>\*</sup> a choice which is statistically more relevant relative to stochastically chosen snapshots

QM/MM calculations, in Figures 6a and 6b, show that the ground state of **HM1** is the doublet state. The reaction barrier is also lower than in the sextet state and the reaction is hence spin-selective (>99%). Clearly therefore the box modifies the intrinsic properties of the captive **HM1**.

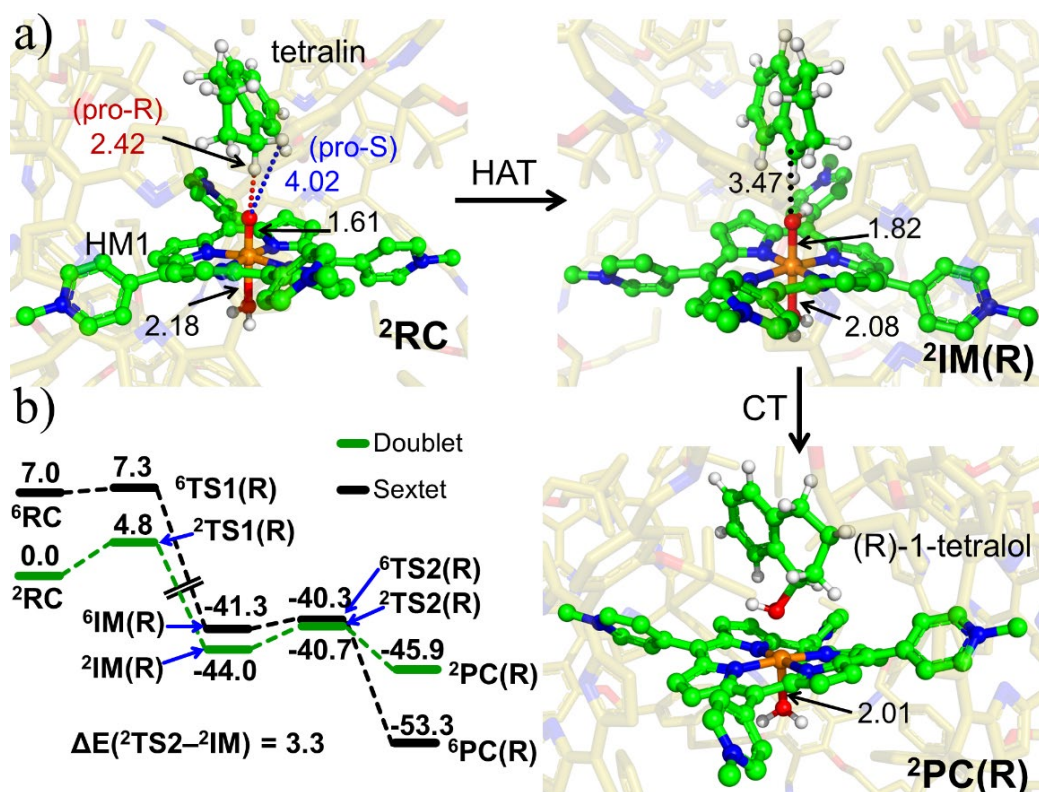


**Figure 6.** (a) The key geometric data as well as QM/MM optimized geometries of  ${}^2\text{RC}$ ,  ${}^2\text{IM}(\text{R})$  and  ${}^2\text{PC}(\text{R})$ . The optimized geometries of  ${}^2\text{TS1}(\text{R})$ ,  ${}^2\text{TS2}(\text{R})$  and for the corresponding sextet state species can be found in SI, Figure S7 & S8. (b) The complete ZPE corrected QM/MM/UB3LYP/def2-TZVP reaction profile diagram for the *R*-enantioselective C-H hydroxylation of tetralin into (*R*)-1-tetralol by active oxidant **HM1** entrapped inside the modelled cage. All the calculations have been performed for both doublet and sextet states. Distances are in Å, and energies are reported in kcal·mol<sup>-1</sup> relative to RC.

Furthermore, it is seen that the H-transfer energy barrier is merely 4.8 kcal/mol, and the process is preferred for the pro-*R* H-abstraction. Notably, the reaction is mediated by **IM1**, which involves a tetralinyl cation and Fe(III)-OH<sup>-</sup> heme species. Subsequently, the substrate cation attacks the Fe-OH bond and generates the *R*-tetralol product. By comparison, the pro-*S* H-abstraction barrier is 7.81 kcal·mol<sup>-1</sup> (see SI, Figure S9 & S10). Based on the energy barrier

difference, the *R/S* ratio at 298.15 K, corresponds to 159:1 for *R/S* enantio-selectivity of the Tetralol (see SI, Figure S9). Clearly the cage modifies both the reactivity and enantioselectivity of **HM1**.

In contrast to the previous study with **HM1**,<sup>22</sup> here there is no spin crossover during the H-transfer step, since the reaction prefers to occur almost exclusively on the doublet state surface. Thus, the cage environment perturbs the electronic states and creates a preference for the doublet state. At the same time, the final *R*-alcohol product is most stable in the sextet state, as happens in many reactions of P450.<sup>68</sup>

**The mechanism of the oxidation reaction and the role of LEF:** To decipher the reaction mechanism, we studied the electronic structures of all stationary species with spin doublet. As can be seen from Figure 7a, in the free oxidant, the three unpaired electrons are populated on **HM1**, much the same as in the standard electronic structure of porphyrin radical-cation coupled to a triplet oxo-iron moiety to a total of a doublet spin. However, in the presence of tetralin (**TLN**) entrapped inside the cage, an electron is transferred from **TLN** (Figure 7b) to the singly occupied orbital of the **HM1**<sup>+</sup> species. *This electron transfer occurs due to the LEF of the cage that drives an electron from TLN to HM1.* A complete mechanism of the reaction is depicted in Figure 7c. As can be seen, the reaction begins with a single electron transfer from the electron-rich **TLN** substrate to **HM1**, to yield the **RC**, followed by a hydrogen transfer to the oxo-iron complex, and finally, the **TLN**-cation rebounds on the hydroxo-iron complex and yields the Tetralol product.

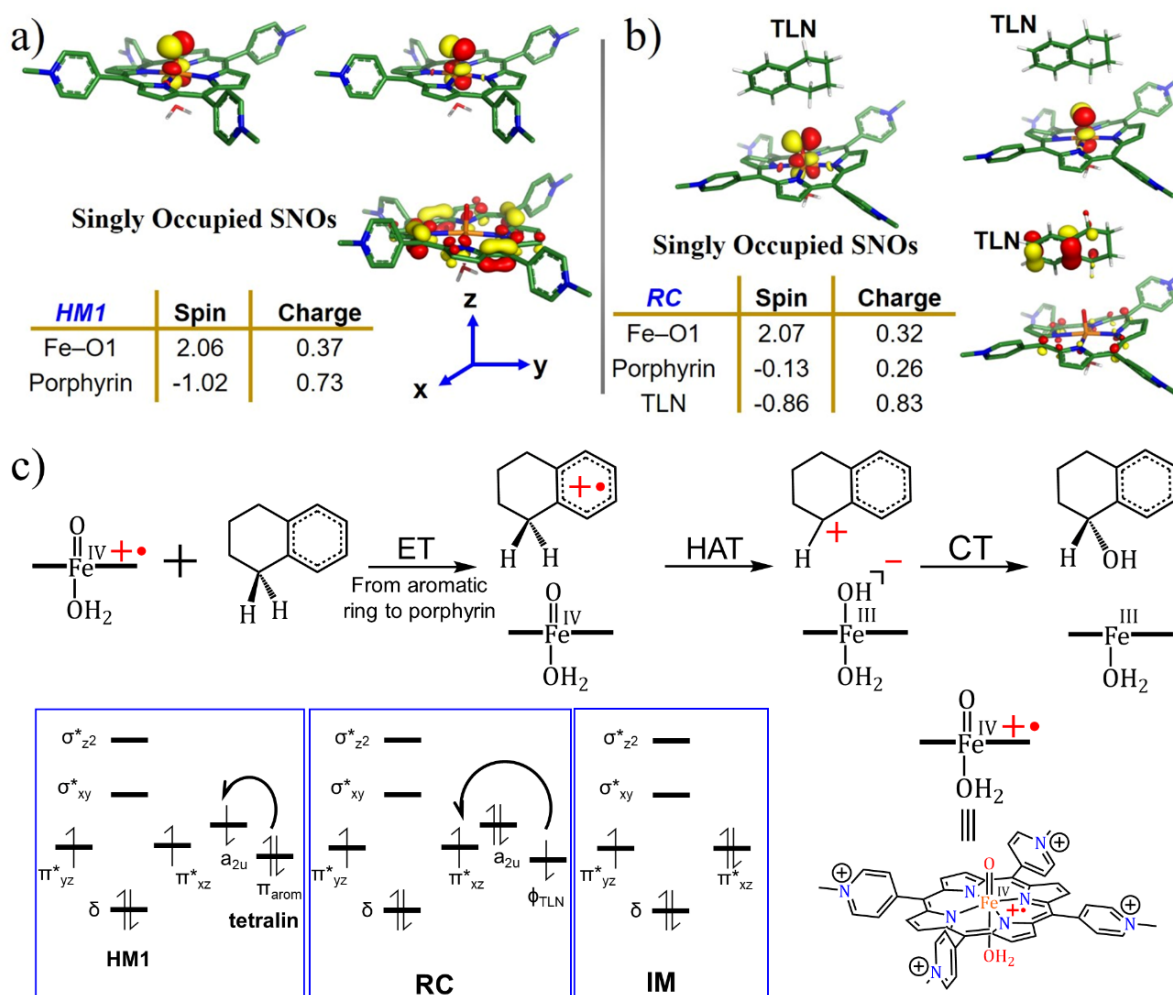


**Figure 7.** The spin natural orbitals (SNOs), Mulliken spin density and charges for (a) lone active oxidant HM1 and (b) Reactant Cluster, RC. TLN refers to the substrate tetralin. All the electronic structure calculations were carried out for the doublet ground state of the complex. (c) A complete reaction mechanism along with the orbital occupation during reaction. See SI for Mulliken spin density and charges, Table S1.

To substantiate the role of the LEF, we quantify in Figure 8 the LEF exerted by the cage along the reaction axis using the TITAN program. As we can see, the LEF significantly stabilizes the TS state for the *R* enantio-selectivity compared with the TS for the *S* enantio-selectivity.

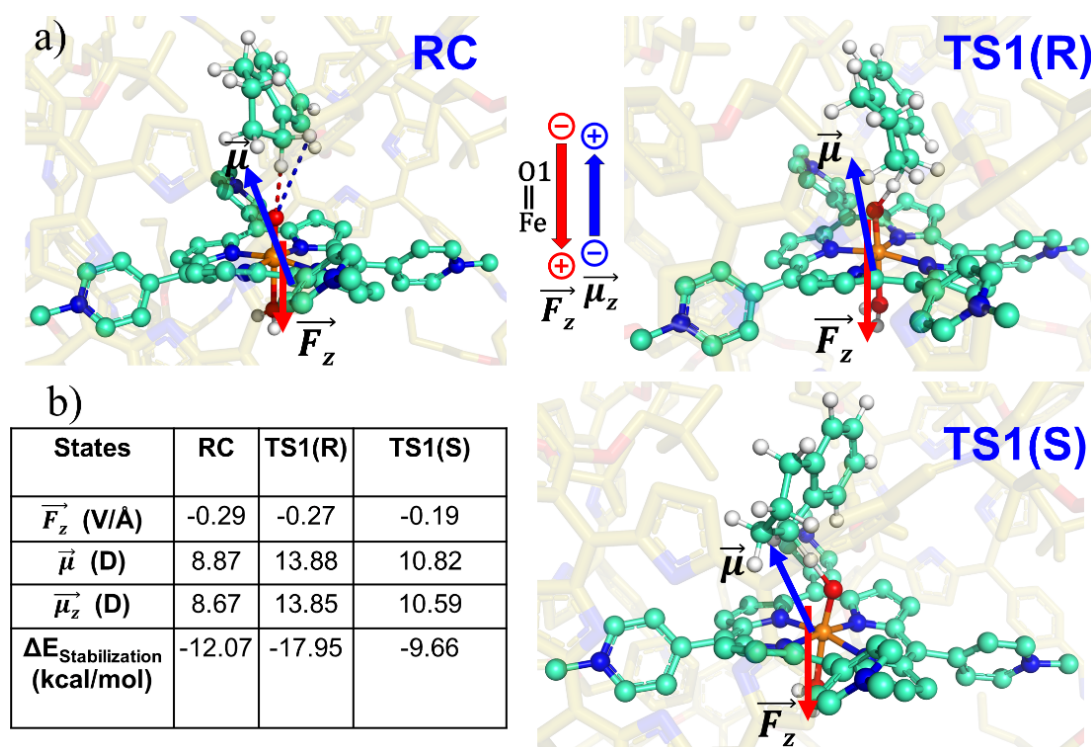


**Figure 8.** a) RC, TS1-*R* and TS1-*S* states showing the direction of local electric field (LEF) and dipole moment. (b) Calculated  $\text{LEF}_z$ , dipole moments, and stabilization energies. Note that we have a GAUSSIAN convention to define the direction of electric fields and dipole moments. Dipole moments have been calculated for  $\text{H}_2\text{O-Fe=O}$ , porphyrin and TLN.

**Is the LEF responsible for the initial electron transfer (ET)?** To ascertain the role of the LEF on the initiation of the hydroxylation via an electron transfer from Tetralin to Cpd I, we removed the cage and methyl substitutions of the **HM1** from the optimized **RC** complex to mimic a zero-field environment. Thereafter, we performed a single-point calculation of the **RC** and its singly occupied SNOs for the reactant geometry (see SI for Mulliken spin density and charges, Table S2). Our calculations revealed that in the absence of the LEF, **HM1** retains its electrons and so does the substrate **TLN** (see Figure 9A). As such, ET does not occur in the absence of the LEF of the cage. We then applied an external electric field (EEF) of similar magnitude as the LEF exerted by the cage and substituted **HM1** (the original **RC**). Consequently, now an electron is extracted from the substrate and regenerates an electronic structure which is in line with the one observed by using the modeled-cage scenario (see Figure

9B). This provides compelling evidence that it is the LEF of the system that mediates the initial ET step, leading to the generation of RC, and subsequently, the reaction proceeds quickly.

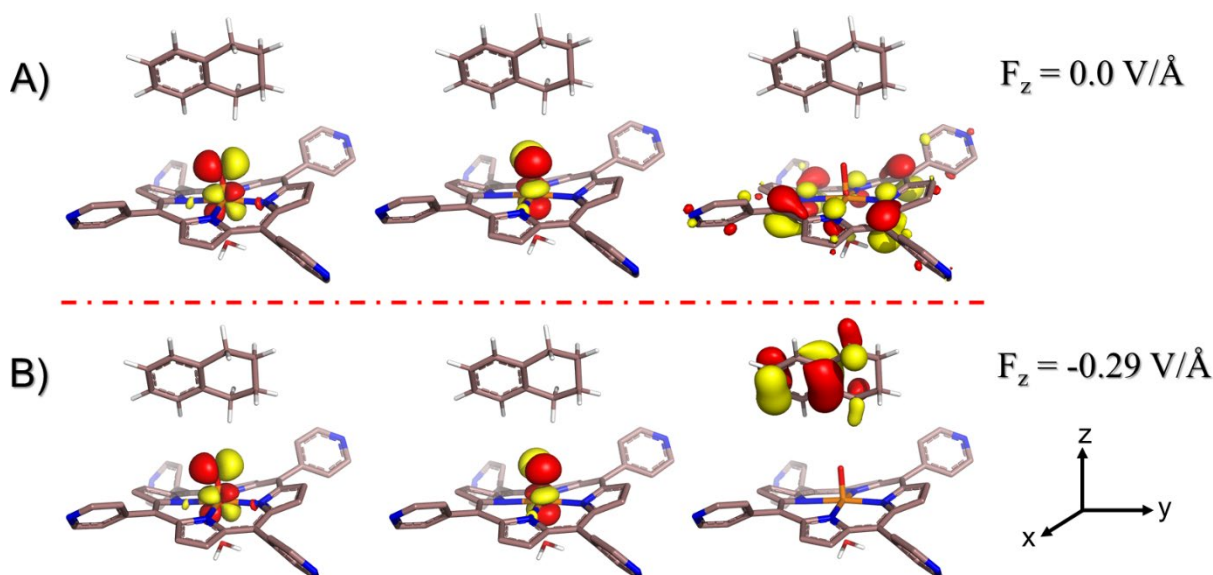


**Figure 9.** Singly occupied spin natural orbitals (SNOs) for demethylated (uncharged) RC doppelganger; (A) in the absence of any externally oriented electric field, (B) in the presence of the oriented external electric field of intensity  $-0.29 \text{ V/\AA}$  projected along with the F–O axis (negative z-axis) of the same order of magnitude exerted by the combination of the modelled cage and the pyridinium periphery as estimated from the QM/MM optimized geometry. Note that for electric field direction, the GAUSSIAN convention is used. The arrows at the right bottom represent the cartesian axis. All the electronic structure calculations were carried out for the doublet ground state of the complex.

**Does the LEF also regulate the *R/S* enantioselectivity?** To probe the origins of the reaction's enantioselectivity, we computed the LEF along the y-axis for RC, TS1(R), and TS2(S) (see Table 1). The LEF was found to be directed along positive y-axis for all the species. At the same time, the dipole moment for TS1(R) is aligned along the stabilizing direction vis-à-vis the LEF.

Let us then proceed with the calculation of stabilization energy of the two chiral isomers of the TS in the presence of the 2D-LEF. For this purpose, we employ the following relationship:

$$\Delta E = 4.8 |\vec{F}| \cdot |\vec{\mu}| \cdot \cos\theta$$

Here,  $\Delta E$  is stabilization/destabilization energy in kcal/mol,  $|\vec{F}|$  is the LEF intensity in V/Å, the  $|\vec{\mu}|$  is the magnitude of dipole moment in Debye and  $\theta$  is the angle between LEF and dipole moment vectors. The results are collected in Table 1.

**Table 1.** Total dipole moment  $\mu$  and their x, y- components. Local Electric Field (LEF) along y- and z- axis and their contributions for electrostatic stabilization for different states. Note that GAUSSIAN conversion is used to define direction of electric field and dipole moment; and iron-oxo, porphyrin, & substrate are used for dipole moment calculation.

States	$ \vec{\mu} $ (D)	$ \vec{F}_z $ (V/Å)	$\vec{\mu}_z$ (D)	$\Delta E_z$ (kcal/mol)	$ \vec{F}_y $ (V/Å)	$\vec{\mu}_y$ (D)	$\Delta E_y$ (kcal/mol)
RC	8.87	-0.29	8.67	-12.07	0.19	1.76	1.61
TS1(R)	13.88	-0.27	13.85	-17.95	0.20	-0.40	-0.32
TS1(S)	10.82	-0.19	10.59	-9.66	0.23	1.66	1.84

Table 1 reveals that the TS1(R) is better aligned than TS1(S) in the direction of the LEF, and it possesses relatively higher dipole moments along the y- and z-axes. As such, this dipole moment of TS1(R) will interact more strongly with the LEF than TS1(S), which possesses a lower z-LEF and higher y-EEF which is misoriented and destabilizes this TS. As such, the pro-S TS is less stabilized compared with the pro-R TS. The interaction energy calculations predict that the two directional electric fields complement each other for the reactivity and the selectivity. Clearly therefore, the LEF of the system is the decisive factor for the exclusive R-selective pathway and for its enhanced reactivity. This was further supported by a separate calculation, in which we stripped the cage and charged substitution, and found no enantioselectivity (see SI, Figure S11).

### 3.3 Can the LEF of the supramolecular cage be tweaked to get enantioselectivity at will?

Since a y-directional electric field in our cage causes *R*-enantioselective reaction, we set out to reverse the LEF of the cage (see SI, Figure S12) and produce *S*-enantioselectivity. Figure 10 shows that when we place a charged substituent in the negative y-direction (mod1), we achieve an absolute *R* enantio-selectivity. In contrast, when we place the same charged substitution on the positive y-direction (mod2), the reaction becomes *S*-enantioselective. *Therefore, simply flipping the direction of the designed LEF in the supramolecular cages creates absolute enantioselectivity at will!*

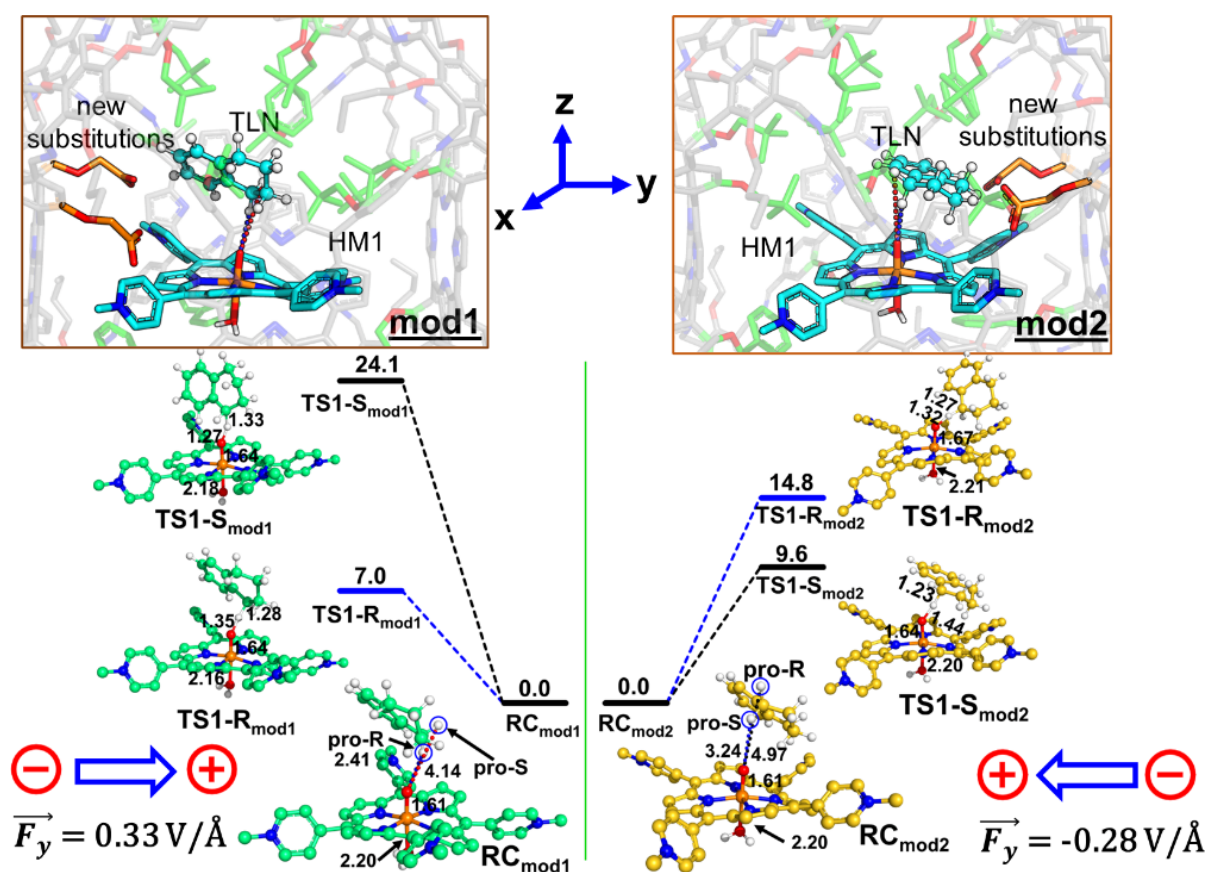


**Figure 10.** The ZPE corrected QM/MM/UB3LYP/def2-TZVP reaction profile diagram along with the optimized structures and key geometric data for *mod1* and *mod2* cages. PES scanning for HAT has been performed for the doublet ground state of the complex. Distances are in Å, and energies are reported in kcal·mol<sup>-1</sup> relative to RC. The gaussian convention is used for electric field vectors.

### 3.4 Entry/Exit of the Substrate/Product

To investigate the process of substrate/product binding and unbinding, we employed adaptive steered molecular dynamics (ASMD) simulation and calculated the potential of mean force (PMF) using the Jarzynski average<sup>67</sup>. Previous studies has shown that the PMF values qualitatively fit with the theoretical and experimental binding free energy calculations.<sup>69</sup> The results of this calculation are illustrated in Figure 11a, with PMF values of ~15.5 and ~15.9 kcal/mol for the substrate (tetralin) and the hydroxylated product (*R*-1-tetralol), respectively. The smaller values of free energies as observed by the PMF plot show a feasible substrate entry and exit from the supramolecular cage.

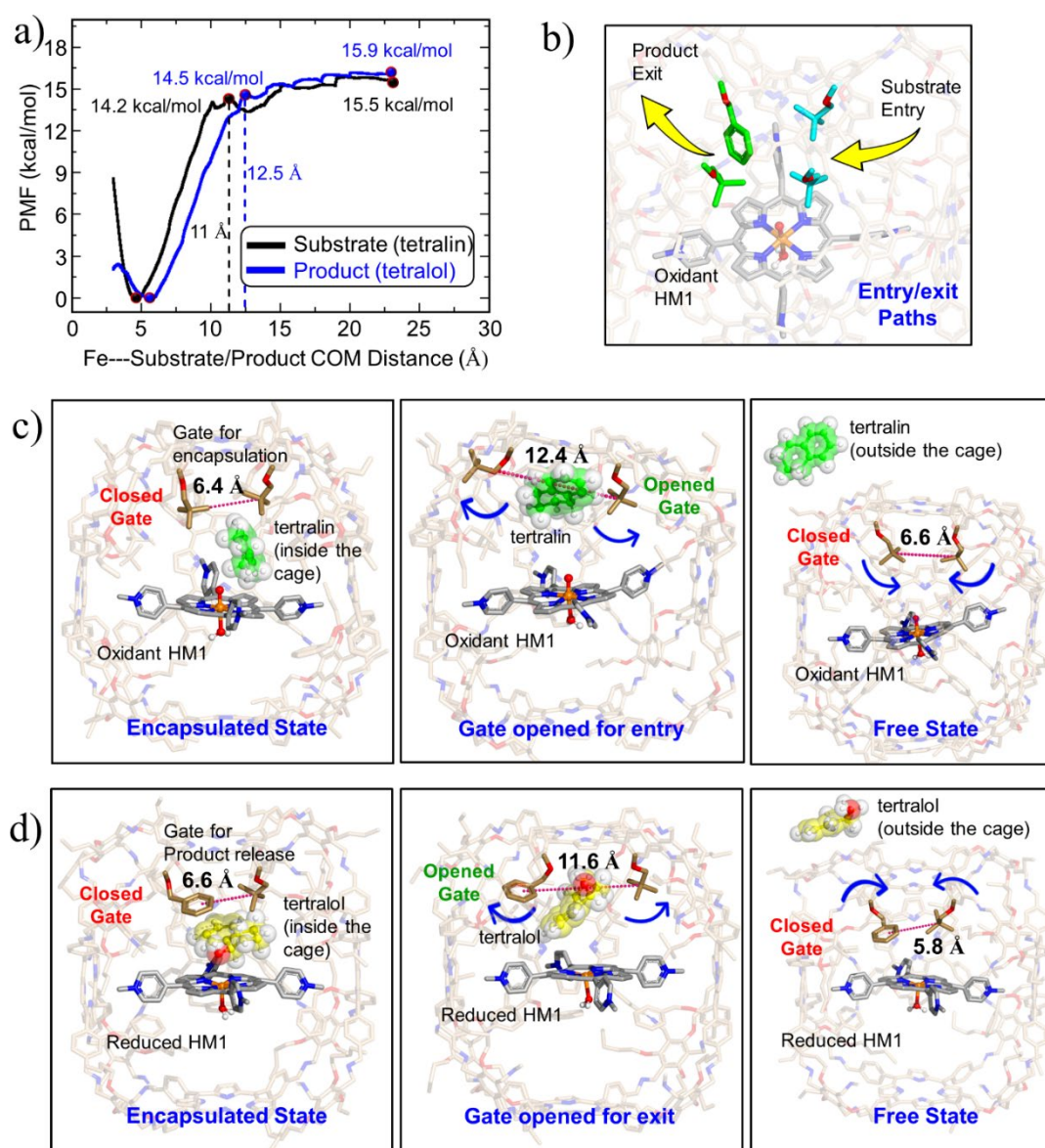


**Figure 11.** (a) ASMD derived PMF along the reaction coordinate for both, substrate & hydroxylated product. (b) Obtained paths for substrate entry and product exit from the cage. (c,d) Representative states for unbinding/binding process for substrate and product, respectively. The distances for the movement of crucial groups are in SI, Figure S13.

During the exit, we observe a sharp increase in the PMF, i.e., free energy for both substrate and product as they dissociate from the active site. The rise in PMF is mainly due to the force against the hydrophobic interactions (SI, Figure S5) between substrate and cage-substituents when substrate/product moves from 3 to 10-12 Å from the reactive center, i.e., Fe=O for HM1. Interestingly, we observed that both t-butyl groups and the phenyl substitution of the cage act as *doorways which can easily be shuttles from open to close conformation to allow the substrate entry and the product exit* (Figure 11b-d). Interestingly, once substrate enters or product exists the cage, the two t-butyl groups and the phenyl groups, restore their previous orientations, indicating an important dynamics during the entry/exit of the substrate/product. As can be seen, the PMF becomes linear after the substrate/product dissociates the cage at 23 Å indicating no further force is applied. *The total work (PMF) implies that the substrate can easily access the active oxidant inside the modeled cage, while the hydroxylated product can escape and leave the space.* These findings shed light on the energetics and dynamics of the substrate/product dissociation process and have important implications for the design and optimization of supramolecular cages for catalytic applications.

#### 4. Conclusions

In the present work, we demonstrate that a methodological design of LEF in a supramolecular cage brings about the desired reactivity and selectivity of C-H hydroxylation reactions. Using rational designing principles, the supramolecular cage can be strategically modified to entrap the desired product. Furthermore, the designed local electric field lateral to the reaction axis

provides absolute enantioselectivity of the product, and it can be tailored to produce the desired enantioselectivity. Finally, the LEF along the reaction axis can readily facilitate the electron transfer process, which in turn, enhances the reactivity several fold.

As such, the present work demonstrates a new state-of-art catalyst design which is sustainable and recyclable for different product formations.

**5. Acknowledgments:** KDD acknowledges the Department of Biotechnology, Ministry of Science and Technology, Govt. of India for the Ramalingaswami re-entry grant (BT/RLF/Re-entry/10/2017). SS is supported by the Israel Science Foundation (grant 520/18).

## 6. References:

- (1) Greenaway, R. L.; Santolini, V.; Bennison, M. J.; Alston, B. M.; Pugh, C. J.; Little, M. A.; Miklitz, M.; Eden-Rump, E. G. B.; Clowes, R.; Shakil, A.; Cuthbertson, H. J.; Armstrong, H.; Briggs, M. E.; Jelfs, K. E.; Cooper, A. I. High-Throughput Discovery of Organic Cages and Catenanes Using Computational Screening Fused with Robotic Synthesis. *Nat. Commun.* **2018**, *9* (1), 1–11.
- (2) Berardo, E.; Greenaway, R. L.; Turcani, L.; Alston, B. M.; Bennison, M. J.; Miklitz, M.; Clowes, R.; Briggs, M. E.; Cooper, A. I.; Jelfs, K. E. Computationally-Inspired Discovery of an Unsymmetrical Porous Organic Cage. *Nanoscale* **2018**, *10* (47), 22381–22388.
- (3) Piskorz, T. K.; Martí-Centelles, V.; Young, T. A.; Lusby, P. J.; Duarte, F. Computational Modeling of Supramolecular Metallo-Organic Cages-Challenges and Opportunities. *ACS Catal.* **2022**, 5806–5826.

- (4) Montà-González, G.; Sancenón, F.; Martínez-Mañez, R.; Martí-Centelles, V. Purely Covalent Molecular Cages and Containers for Guest Encapsulation. *Chem. Rev.* **2022**, *122* (16), 13636–13708.
- (5) Slater, A. G.; Reiss, P. S.; Pulido, A.; Little, M. A.; Holden, D. L.; Chen, L.; Chong, S. Y.; Alston, B. M.; Clowes, R.; Haranczyk, M.; Briggs, M. E.; Hasell, T.; Day, G. M.; Cooper, A. I. Computationally-Guided Synthetic Control over Pore Size in Isostructural Porous Organic Cages. *ACS Cent. Sci.* **2017**, *3* (7), 734–742.
- (6) Durand, D. J.; Fey, N. Computational Ligand Descriptors for Catalyst Design. *Chem. Rev.* **2019**, *119* (11), 6561–6594.
- (7) Wang, X.; Zhang, G.; Yang, L.; Sharman, E.; Jiang, J. Material Descriptors for Photocatalyst/Catalyst Design. *Wiley Interdiscip. Rev. Comput. Mol. Sci.* **2018**, *8* (5), e1369.
- (8) Hülsey, M. J.; Lim, C. W.; Yan, N. Promoting Heterogeneous Catalysis beyond Catalyst Design. *Chem. Sci.* **2020**, *11* (6), 1456–1468.
- (9) Roca, M.; Liu, H.; Messer, B.; Warshel, A. On the Relationship between Thermal Stability and Catalytic Power of Enzymes. *Biochemistry* **2007**, *46* (51), 15076–15088.
- (10) Feller, G. Protein Stability and Enzyme Activity at Extreme Biological Temperatures. *J. Phys. Condens. Matter* **2010**, *22* (32), 323101.
- (11) Ji, Q.; Xiao, S.; He, B.; Liu, X. Purification and Characterization of an Organic Solvent-Tolerant Lipase from *Pseudomonas Aeruginosa* LX1 and Its Application for Biodiesel Production. *J. Mol. Catal. B Enzym.* **2010**, *66* (3–4), 264–269.
- (12) Sharma, S.; Kanwar, S. S. Organic Solvent Tolerant Lipases and Applications. *Sci.*

*World J.* **2014**, 2014.

- (13) Marin-Argany, M.; Güell-Bosch, J.; Blancas-Mejía, L. M.; Villegas, S.; Ramirez-Alvarado, M. Mutations Can Cause Light Chains to Be Too Stable or Too Unstable to Form Amyloid Fibrils. *Protein Sci.* **2015**, *24* (11), 1829–1840.
- (14) Guo, H. H.; Choe, J.; Loeb, L. A. Protein Tolerance to Random Amino Acid Change. *Proc. Natl. Acad. Sci.* **2004**, *101* (25), 9205–9210.
- (15) Taverna, D. M.; Goldstein, R. A. Why Are Proteins Marginally Stable? *Proteins Struct. Funct. Bioinforma.* **2002**, *46* (1), 105–109.
- (16) Nguyen, Q. N. N.; Xia, K. T.; Zhang, Y.; Chen, N.; Morimoto, M.; Pei, X.; Ha, Y.; Guo, J.; Yang, W.; Wang, L.-P. Source of Rate Acceleration for Carbocation Cyclization in Biomimetic Supramolecular Cages. *J. Am. Chem. Soc.* **2022**, *144* (25), 11413–11424.
- (17) Hong, S.; Rohman, M. R.; Jia, J.; Kim, Y.; Moon, D.; Kim, Y.; Ko, Y. H.; Lee, E.; Kim, K. Porphyrin Boxes: Rationally Designed Porous Organic Cages. *Angew. Chemie - Int. Ed.* **2015**, *54* (45), 13241–13244.
- (18) Hasell, T.; Cooper, A. I. Porous Organic Cages: Soluble, Modular and Molecular Pores. *Nat. Rev. Mater.* **2016**, *1* (9).
- (19) Zhang, J. H.; Xie, S. M.; Zi, M.; Yuan, L. M. Recent Advances of Application of Porous Molecular Cages for Enantioselective Recognition and Separation. *J. Sep. Sci.* **2020**, *43* (1), 134–149.
- (20) Vaissier Welborn, V.; Head-Gordon, T. Electrostatics Generated by a Supramolecular Capsule Stabilizes the Transition State for Carbon-Carbon Reductive Elimination from Gold(III) Complex. *J. Phys. Chem. Lett.* **2018**, *9* (14), 3814–3818.

- (21) Warshel, A.; Sharma, P. K.; Kato, M.; Parson, W. W. Modeling Electrostatic Effects in Proteins. *Biochim. Biophys. Acta (BBA)-Proteins Proteomics* **2006**, *1764* (11), 1647–1676.
- (22) Stuyver, T.; Ramanan, R.; Mallick, D.; Shaik, S. Oriented (Local) Electric Fields Drive the Millionfold Enhancement of the H-Abstraction Catalysis Observed for Synthetic Metalloenzyme Analogues. *Angew. Chemie* **2020**, *132* (20), 7989–7994.
- (23) Dubey, K. D.; Stuyver, T.; Shaik, S. Local Electric Fields: From Enzyme Catalysis to Synthetic Catalyst Design. *J. Phys. Chem. B* **2022**.
- (24) Fried, S. D.; Boxer, S. G. Electric Fields and Enzyme Catalysis. *Annu. Rev. Biochem.* **2017**, *86*, 387.
- (25) Bím, D.; Alexandrova, A. N. Local Electric Fields as a Natural Switch of Heme-Iron Protein Reactivity. *ACS Catal.* **2021**, *11* (11), 6534–6546.
- (26) Sebastiani, F.; Bender, T. A.; Pezzotti, S.; Li, W.-L.; Schwaab, G.; Bergman, R. G.; Raymond, K. N.; Toste, F. D.; Head-Gordon, T.; Havenith, M. An Isolated Water Droplet in the Aqueous Solution of a Supramolecular Tetrahedral Cage. *Proc. Natl. Acad. Sci.* **2020**, *117* (52), 32954–32961.
- (27) Siddiqui, S. A.; Dubey, K. D. Can the Local Electric Field Be a Descriptor of Catalytic Activity? A Case Study on Chorismate Mutase. *Phys. Chem. Chem. Phys.* **2022**, *24* (4), 1974–1981.
- (28) Yadav, S.; Shaik, S.; Siddiqui, S. A.; Kalita, S.; Dubey, K. D. Local Electric Fields Dictate Function: The Different Product Selectivities Observed for Fatty Acid Oxidation by Two Deceptively Very Similar P450-Peroxygenases OleT and BS $\beta$ . *J. Chem. Inf. Model.* **2022**, *62* (4), 1025–1035.

- (29) English, N. J. Molecular Dynamics in the Presence of External Electric Fields. In *Effects of Electric Fields on Structure and Reactivity*; 2021; pp 263–316.
- (30) Blyth, M. T.; Coote, M. L. Recent Advances in Designed Local Electric Fields. *Eff. Electr. Fields Struct. React.* **2021**, 119–146.
- (31) Shaik, S.; Danovich, D.; Dubey, K. D.; Stuyver, T. The Impact of Electric Fields on Chemical Structure and Reactivity. In *Effects of Electric Fields on Structure and Reactivity*; 2021; pp 12–70.
- (32) Li, H.; Su, T. A.; Zhang, V.; Steigerwald, M. L.; Nuckolls, C.; Venkataraman, L. Electric Field Breakdown in Single Molecule Junctions. *J. Am. Chem. Soc.* **2015**, *137* (15), 5028–5033.
- (33) Shaik, S.; Mandal, D.; Ramanan, R. Oriented Electric Fields as Future Smart Reagents in Chemistry. *Nat. Chem.* **2016**, *8* (12), 1091–1098.
- (34) Wang, Z.; Danovich, D.; Ramanan, R.; Shaik, S. Oriented-External Electric Fields Create Absolute Enantioselectivity in Diels–Alder Reactions: Importance of the Molecular Dipole Moment. *J. Am. Chem. Soc.* **2018**, *140* (41), 13350–13359.
- (35) Dutta Dubey, K.; Stuyver, T.; Kalita, S.; Shaik, S. Solvent Organization and Rate Regulation of a Menshutkin Reaction by Oriented External Electric Fields Are Revealed by Combined MD and QMMM Calculations. *J. Am. Chem. Soc.* **2020**, *142* (22), 9955–9965.
- (36) Shaik, S.; Danovich, D.; Joy, J.; Wang, Z.; Stuyver, T. Electric-Field Mediated Chemistry: Uncovering and Exploiting the Potential of (Oriented) Electric Fields to Exert Chemical Catalysis and Reaction Control. *J. Am. Chem. Soc.* **2020**, *142* (29), 12551–12562.

- (37) Aragonés, A. C.; Haworth, N. L.; Darwish, N.; Ciampi, S.; Bloomfield, N. J.; Wallace, G. G.; Diez-Perez, I.; Coote, M. L. Electrostatic Catalysis of a Diels–Alder Reaction. *Nature* **2016**, *531* (7592), 88–91.
- (38) Shaik, S.; Ramanan, R.; Danovich, D.; Mandal, D. Structure and Reactivity/Selectivity Control by Oriented-External Electric Fields. *Chem. Soc. Rev.* **2018**, *47* (14), 5125–5145.
- (39) Foroutan-Nejad, C.; Marek, R. Potential Energy Surface and Binding Energy in the Presence of an External Electric Field: Modulation of Anion– $\pi$  Interactions for Graphene-Based Receptors. *Phys. Chem. Chem. Phys.* **2014**, *16* (6), 2508–2514.
- (40) Bell, S. R.; Groves, J. T. A Highly Reactive P450 Model Compound I. *J. Am. Chem. Soc.* **2009**, *131* (28), 9640–9641.
- (41) Smith, P. T.; Benke, B. P.; An, L.; Kim, Y.; Kim, K.; Chang, C. J. A Supramolecular Porous Organic Cage Platform Promotes Electrochemical Hydrogen Evolution from Water Catalyzed by Cobalt Porphyrins. *ChemElectroChem* **2021**, *8* (9), 1653–1657.
- (42) Yusran, Y.; Fang, Q.; Qiu, S. Postsynthetic Covalent Modification in Covalent Organic Frameworks. *Isr. J. Chem.* **2018**, *58* (9), 971–984.
- (43) Wang, H.; Jin, Y.; Sun, N.; Zhang, W.; Jiang, J. Post-Synthetic Modification of Porous Organic Cages. *Chem. Soc. Rev.* **2021**, *50* (16), 8874–8886.
- (44) Kalay, E.; Şahin, E. Biocatalytic Asymmetric Synthesis of (R)-1-tetralol Using *Lactobacillus Paracasei* BD101. *Chirality* **2021**, *33* (8), 447–453.
- (45) Mayhew, M. P.; Roitberg, A. E.; Tewari, Y.; Holden, M. J.; Vanderah, D. J.; Vilker, V. L. Benzocycloarene Hydroxylation by P450 Biocatalysis. *New J. Chem.* **2002**, *26* (1),

- 35–42.
- (46) Yang, Y.; Boehman, A. L. Oxidation Chemistry of Cyclic Hydrocarbons in a Motored Engine: Methylcyclopentane, Tetralin, and Decalin. *Combust. Flame* **2010**, *157* (3), 495–505.
- (47) Dewar, M. J. S.; Zoebisch, E. G.; Healy, E. F.; Stewart, J. J. P. Development and Use of Quantum Mechanical Molecular Models. 76. AM1: A New General Purpose Quantum Mechanical Molecular Model. *J. Am. Chem. Soc.* **1985**, *107* (13), 3902–3909.
- (48) Vassetz, D.; Pagliai, M.; Procacci, P. Assessment of GAFF2 and OPLS-AA General Force Fields in Combination with the Water Models TIP3P, SPCE, and OPC3 for the Solvation Free Energy of Druglike Organic Molecules. *J. Chem. Theory Comput.* **2019**, *15* (3), 1983–1995.
- (49) Li, P.; Merz Jr, K. M. MCPB. Py: A Python Based Metal Center Parameter Builder. ACS Publications 2016.
- (50) Cornell, W. D.; Cieplak, P.; Bayly, C. I.; Kollman, P. A. Application of RESP Charges to Calculate Conformational Energies, Hydrogen Bond Energies, and Free Energies of Solvation. *J. Am. Chem. Soc.* **2002**, *115* (21), 9620–9631.
- (51) Bayly, C. I.; Cieplak, P.; Cornell, W.; Kollman, P. A. A Well-Behaved Electrostatic Potential Based Method Using Charge Restraints for Deriving Atomic Charges: The RESP Model. *J. Phys. Chem.* **1993**, *97* (40), 10269–10280.
- (52) Ryckaert, J.-P.; Ciccotti, G.; Berendsen, H. J. C. Numerical Integration of the Cartesian Equations of Motion of a System with Constraints: Molecular Dynamics of n-Alkanes. *J. Comput. Phys.* **1977**, *23* (3), 327–341.

- (53) Darden, T.; York, D.; Pedersen, L. Particle Mesh Ewald: An  $N \cdot \log(N)$  Method for Ewald Sums in Large Systems. *J. Chem. Phys.* **1993**, *98* (12), 10089–10092.
- (54) Salomon-Ferrer, R.; Gotz, A. W.; Poole, D.; Le Grand, S.; Walker, R. C. Routine Microsecond Molecular Dynamics Simulations with AMBER on GPUs. 2. Explicit Solvent Particle Mesh Ewald. *J. Chem. Theory Comput.* **2013**, *9* (9), 3878–3888.
- (55) Sherwood, P.; De Vries, A. H.; Guest, M. F.; Schreckenbach, G.; Catlow, C. R. A.; French, S. A.; Sokol, A. A.; Bromley, S. T.; Thiel, W.; Turner, A. J.; Billeter, S.; Terstegen, F.; Thiel, S.; Kendrick, J.; Rogers, S. C.; Casci, J.; Watson, M.; King, F.; Karlsen, E.; Sjøvoll, M.; Fahmi, A.; Schäfer, A.; Lennartz, C. QUASI: A General Purpose Implementation of the QM/MM Approach and Its Application to Problems in Catalysis. *J. Mol. Struct. THEOCHEM* **2003**, *632* (1–3), 1–28.
- (56) Metz, S.; Kästner, J.; Sokol, A. A.; Keal, T. W.; Sherwood, P. ChemShell—a Modular Software Package for QM/MM Simulations. *Wiley Interdiscip. Rev. Comput. Mol. Sci.* **2014**, *4* (2), 101–110.
- (57) Balasubramani, S. G.; Chen, G. P.; Coriani, S.; Diedenhofen, M.; Frank, M. S.; Franzke, Y. J.; Furche, F.; Grotjahn, R.; Harding, M. E.; Hättig, C.; Hellweg, A.; Helmich-Paris, B.; Holzer, C.; Huniar, U.; Kaupp, M.; Marefat Khah, A.; Karbalaeei Khani, S.; Müller, T.; Mack, F.; Nguyen, B. D.; Parker, S. M.; Perlt, E.; Rappoport, D.; Reiter, K.; Roy, S.; Rückert, M.; Schmitz, G.; Sierka, M.; Tapavicza, E.; Tew, D. P.; Van Wüllen, C.; Voora, V. K.; Weigend, F.; Wodyński, A.; Yu, J. M. TURBOMOLE: Modular Program Suite for Ab Initio Quantum-Chemical and Condensed-Matter Simulations. *J. Chem. Phys.* **2020**, *152* (18), 184107.
- (58) Ahlrichs, R.; Bär, M.; Häser, M.; Horn, H.; Kölmel, C. Electronic Structure Calculations

- on Workstation Computers: The Program System Turbomole. *Chem. Phys. Lett.* **1989**, *162* (3), 165–169.
- (59) Smith, W.; Forester, T. R. DL\_POLY\_2. 0: A General-Purpose Parallel Molecular Dynamics Simulation Package. *J. Mol. Graph.* **1996**, *14* (3), 136–141.
- (60) Becke, A. D. Density-functional Thermochemistry. IV. A New Dynamical Correlation Functional and Implications for Exact-exchange Mixing. *J. Chem. Phys.* **1996**, *104* (3), 1040–1046.
- (61) Kästner, J.; Carr, J. M.; Keal, T. W.; Thiel, W.; Wander, A.; Sherwood, P. DL-FIND: An Open-Source Geometry Optimizer for Atomistic Simulations. *J. Phys. Chem. A* **2009**, *113* (43), 11856–11865.
- (62) Ricciardi, G.; Baerends, E. J.; Rosa, A. Charge Effects on the Reactivity of Oxoiron(IV) Porphyrin Species: A DFT Analysis of Methane Hydroxylation by Polycationic Compound i and Compound II Mimics. *ACS Catal.* **2016**, *6* (2), 568–579.
- (63) Stuyver, T.; Huang, J.; Mallick, D.; Danovich, D.; Shaik, S. TITAN: A Code for Modeling and Generating Electric Fields—Features and Applications to Enzymatic Reactivity. *J. Comput. Chem.* **2020**, *41* (1), 74–82.
- (64) Polêto, M. D.; Lemkul, J. A. TUPÃ: Electric Field Analyses for Molecular Simulations. *J. Comput. Chem.* **2022**, *43* (16), 1113–1119.
- (65) Sowlati-Hashjin, S.; Karttunen, M.; Matta, C. F. Electrostatic Fields in Biophysical Chemistry. In *Effects of Electric Fields on Structure and Reactivity*; 2021; pp 225–262.
- (66) Frish, M. J.; Trucks, G. W.; Schlegel, H. B.; Scuseria, G. E.; Robb, M. A.; Cheeseman, J. R.; Scalmani, G.; Barone, V.; Mennucci, B.; Petersson, G. A.; Nakatsuji, H.; Caricato,

M.; Li, X.; Hratchian, H. P.; Izmaylov, A. F.; Bloino, J.; Zheng, G.; Sonnenberg, J. L.; Hada, M.; Ehara, M.; Toyota, K.; Fukuda, R.; Hasegawa, J.; Ishida, M.; Nakajima, T.; Honda, Y.; Kitao, O.; Nakai, H.; Vreven, T.; Montgomery, J. A., Jr.; Peralta, J. E.; Ogliaro, F.; Bearpark, M.; Heyd, J. J.; Brothers, E.; Kudin, K. N.; Staroverov, V. N.; Keith, T.; Kobayashi, R.; Normand, J.; Raghavachari, K.; Rendell, A.; Burant, J. C.; Iyengar, S. S.; Tomasi, J.; Cossi, M.; Rega, N.; Millam, J. M.; Klene, M.; Knox, J. E.; Cross, J. B.; Bakken, V.; Adamo, C.; Jaramillo, J.; Gomperts, R.; Stratmann, R. E.; Yazyev, O.; Austin, A. J.; Cammi, R.; Pomelli, C.; Ochterski, J. W.; Martin, R. L.; Morokuma, K.; Zakrzewski, V. G.; Voth, G. A.; Salvador, P.; Dannenberg, J. J.; Dapprich, S.; Daniels, A. D.; Farkas, O.; Foresman, J. B.; Ortiz, J. V.; Cioslowski, J.; Fox, D. J. Gaussian 09, revision D.01; Gaussian, Inc.: Wallingford, CT, **2013**.

- (67) Jarzynski, C. Nonequilibrium Equality for Free Energy Differences. *Phys. Rev. Lett.* **1997**, *78* (14), 2690.
- (68) Shaik, S.; Cohen, S.; Wang, Y.; Chen, H.; Kumar, D.; Thiel, W. P450 Enzymes: Their Structure, Reactivity, and Selectivity Modeled by QM/MM Calculations. *Chem. Rev.* **2010**, *110* (2), 949–1017.
- (69) Shi, N.; Zheng, Q.; Zhang, H. Molecular Basis of the Recognition of Cholesterol by Cytochrome P450 46A1 along the Major Access Tunnel. *ACS Chem. Neurosci.* **2022**, *13* (10), 1526–1533.